Use of twenty years CLUSTER/FGM data to study the global behavior of the magnetic field and current density of Earth's magnetosphere

P. Robert[1] **and M. Dunlop**[2,3]

[1]Laboratoire de Physique des Plasmas,CNRS, École polytechnique, Palaiseau, France.
[2]School of Space and Environment, Beihang University,100191, Beijing, China.
[3]RAL, Chilton, Oxfordshire, OX11 0QX, UK.

Key Points:

- The twenty years of data from the CLUSTER / FGM magnetometer have been used to constitute a database aligned in time, this has allowed the calculation of curl(B) over the entire duration of the mission.
- A digital magnetic field model, based on a 3-D grid containing experimental averaged values, makes possible the computation of magnetic field lines.
- Position and shape of the cusp has been studied, not only in latitude, but also in longitude, and their geometry visualized by means of the field lines.

Corresponding author: Patrick Robert, `patrick.robert@lpp.polytechnique.fr`

Abstract

The data from the CLUSTER FGM magnetometer, recorded for 20 years at ESA's Cluster Science Archive, as well as the position of the spacecraft, have been used to form a database aligned in time, the 4 s/c flying in formation has allowed the calculation of curl(B) over all the life of the mission (representing the current density via $\mu_0 \vec{J} = \vec{curl} \vec{B}$).

The data of $\vec{B}$ and $\vec{J}$ are then averaged, as a function of the dipole tilt angle, to form a 3D grid of spatial extend of about 20 R_E, and for any spatial resolution.

From these data grids, maps of the direction of the magnetic field and of the current density are produced, allowing the study of the average behavior of the magnetic field and the current density on a large scale.

The validity of the calculation of $\vec{J}$ is discussed. The direction of $\vec{B}$ is used to determine the position and shape of the polar cusps, both in latitude and longitude. It also is possible to propose a simple model of the day-side magnetopause, which we obtain to demonstrate the dataset.

By means of spatial interpolation, the grid is used to provide a digital model of the magnetic field at any point in space where the grid is filled. This model allows ray tracing to be carried out so as to obtain empirical plots of the magnetic field lines, i.e. not theoreti-cal, but from experimental data. In particular, field lines near the cusp bring a direct view of the shape of the cusps. The results are discussed. In a future work it would be possible to add other classification criteria than just the dipole tilt angle, such as various activity indicese and solar wind parameters.The prospect of adding data from other missions would extend the regions that have been covered by Cluster, and in-crease the spatial extent of the 3D grid and its resolution.

1 Introduction

The four CLUSTER S/C have continuously provided excellent data for twenty years, and these data are carefully archived regularly at the CSA of ESA (Laakso et al., 2010). This huge database contains, among other things, the data from the FGM magnetometer (Balogh et al., 1993, 1997; Dunlop et al., 2002). These data are used here to study the global behavior of the magnetic field around the Earth, notably inside the magnetosphere.

In the GSM frame, the form of the mean magnetic field is mainly driven by the value of the dipole tilt angle. The values of the field can be distributed in spatial grids, dependent on this angle. We make the spatial average in each cell of the grid, and then obtain temporal averages over the twenty years of measurements. Of course, we thus erase all the transient effects, but we obtain the value of the mean field in an extended spatial volume, insofar as the orbit of the measurement points makes a complete revolution in this reference frame every year.

The direction and intensity of the field can be studied, in order to determine its overall behavior. CLUSTER allows access to the spatial quantities such as curl(B) and div(B), we calculate the linear approximation to these quantities for all the available values of B, and we set up a large database of curl(B) and div(B) covering these same twenty years.

Average 3-D grids can be calculated , and leads us to visualize interresting informations.

2 Data Access and Processing

2.1 Data Downloading

All FGM data used in this paper were downloaded from the CSA (Laakso et al., 2010) in CEF format (Allen et al., 2004), as well as all satellite position data. The FGM data used are those of "spin resolution", around 4 seconds. Over the 19 years taken into account, 85 984 files have been downloaded. In order to be able to process them with an appropriate software (Robert, 2021) they have been converted into the required format (Robert, 2011) and reach a total volume of 37.6 GB. This base constitutes the starting point for all treatments carried out thereafter.

2.2 Making a Twenty Years CLUSTER Time Aligned Data Base

To calculate rotational and divergence, it is necessary to have the 4 measurements of $\vec{B_{ij}}$ and the 4 positions $\vec{P_{ij}}$ measured at the same time (i=1,3 j=1,4).

Position data are provided every minute, while FGM data are provided approximately every 4 seconds, but the time stamp is not the same on all 4 satellites.

It is therefore necessary to interpolate the values of the field, and to bring them back to the same common time, then to interpolate the positions to have these values at the same times as the magnetic field. So we have established a *'spin resolution time-aligned database'* with the same time base for the 4 satellites, in field and in position, and this for 19 years of data (2001-2019 included).

As it is on this basis that we are going to work, it only contains the fields and the positions, aligned in time, and written in binary to save disk space. It has 25 882 files for a total volume of 20 GB

2.3 Computing Current Density on the Whole Database

On this database, we calculated $\vec{\nabla} \times \vec{B}$ and $\vec{\nabla} \cdot \vec{B}$, for each time stamp, without any particular selection (this will be done later). This is done for each year, and results are written in a binary file, containing date/time, fields and position of each S/C, curl and div of B, as well as Elongation and Planarity parameters (Robert, Roux, et al., 1998), and dipole tilt angle. Table 1 below shows the record number of each yearly file.

year	record	year	record
2001	3379091	2011	6281300
2002	5637934	2012	6128973
2003	7480286	2013	6321965
2004	7186244	2014	6128059
2005	14209733	2015	5450925
2006	7039167	2016	5670593
2007	6828576	2017	6076254
2008	6858573	2018	6275176
2009	6755246	2019	5452257
2010	6360363		
total	125 520 715		

Table 1. Number of value where J is computed

As it is not easy to reread a file of one hundred and twenty five million lines each time you want to do a calculation, five files have been created by region, all in GSM system, see table 2. For meridian or equatorial plane, the thick of selectionned data set is $\pm 1 R_E$. For cusp region,we took a half sphere of thickness $1 R_E$, tengent at the magnetopause .

File	region	records	size GB
XZ.dat	X-Z meridian plane	22142190	3.5
XY.dat	X-Y equatorial plane	16310738	2.6
YZ.dat	Y-Z plane, at X=0	20441846	3.5
YZ17.dat	Y-Z plane, at X=-17R_E	8955949	1.4
Cusp.dat	Near magnetopause, day side	17099642	2.7

Table 2. Data files used to study various regions.

2.3.1 Computation Method

Before attempting to calculate the current densities from experimental data of the fields and positions of the 4 satellites, it is first necessary to ensure that the method used is reliable and does not contain errors.

The calculation method used for the estimation of curl(B) is that of the classical method of contour integrals on each face of the tetrahedron, by applying Ampere's law on each face:

$$\oint \overrightarrow{B}(M).\overrightarrow{dl} = \mu_0.I$$

By choosing 3 faces out of the 4 possible, and after processing to reduce to an orthonormal coordinate system, we thus obtain 4 possible values for the estimation of the rotational. In practice, when the tetrahedron is not degenerate, these 4 values are extremely close, and we use as final result the average of these 4 estimations.

To compute div(B) we use the divergence law, or Green-Ostrogradski law, as:

$$\iiint_{\mathcal{V}} \overrightarrow{\nabla} \cdot \overrightarrow{B}\, \mathrm{d}V = \oint_{\partial \mathcal{V}} \overrightarrow{B} \cdot \mathrm{d}\overrightarrow{S}$$

with $\mu_0 = 4\pi \times 10^{-7} T \cdot m/A$

This method has been used extensively in all of the many curlometer studies applied to CLUSTER's FGM data. Analysis of multipoint magnetometer data appears a long time before Cluster launch (Dunlop et al., 1988, 1990), as well as the influence of the shape of the tetrahedron on the accuracy of the measurement of currents (Robert & Roux, 1990, 1993; Khurana et al., 1996).

Various geometric criteria have been suggested to define the shape of the tetrahedron in relation to the precision of the measurements (Robert, Roux, & Coeur-Joly, 1995; Robert, Roux, & Chanteur, 1995; Robert, Roux, et al., 1998; Robert, Dunlop, et al., 1998; Dunlop et al., 2002; Dunlop & Eastwood, 2008)

Another method to compute Curl and Div was developed by G. Chanteur (Chanteur & Mottez, 1993), based on barycentric coordinates. This elegant method amounts to es-

timate the matrix of gradients, the diagonal terms giving the digergence, while the anti-diagonal terms are used to calculate the rotational (Chanteur, 1998) and (Chanteur & Harvey, 1998) .

2.3.2 Testing the Method

As we have to make a choice beetween the classical method based on Ampere's law, nicknamed the 'curlometer', and the barycentric coordinates, we took the first method, based on a code developed by the author for over 30 years, and which was used and tested on numerous simulated data.

A good code is not enough, for the application to the magnetosphere, it is absolutely necessary to first remove the dipole field, and better, the field given by the IGRF model (Thébault et al., 2015) before applying the calculation (see discussion in Dunlop et al., 2018, 2020) in order to remove the zero current, nonlinear dipole gradients. We can check the absolute necessity of doing this operation on the data simulated by the Tsyganenko field model (Tsyganenko, 1987).

Figure 1 shows the results of the calculation before and after subtraction of the IGRF. If we do not do this operation, the high value of the magnetic field near the Earth completely distorts the results of the calculation.

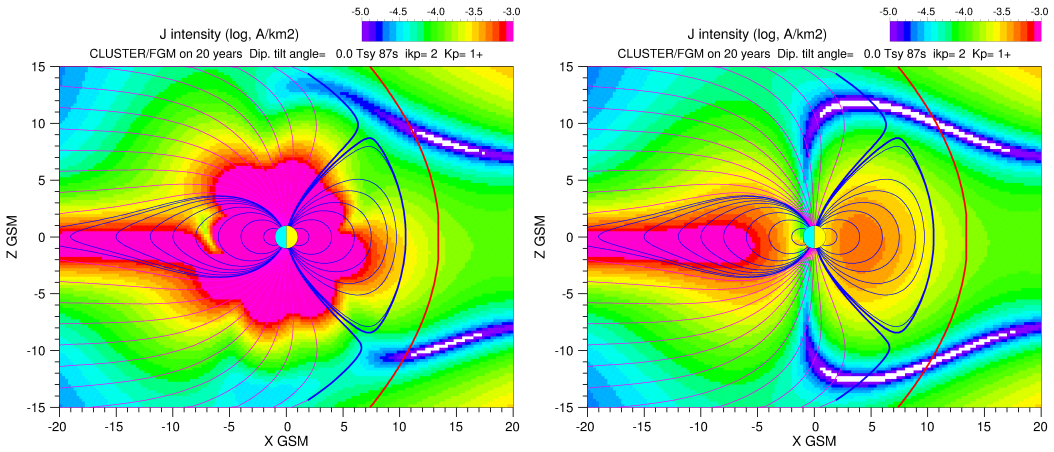

Figure 1. Computation of the current density on T87s model. Left: without removing IGRF field before computation. Right: with removing.

2.3.3 Criteria Used for the Estimate of Curl(B) and Div(B)

When we calculate $\vec{\nabla}\times\vec{B}$ and $\vec{\nabla}\cdot\vec{B}$, we obtain two estimates of these quantities. If the tetrahedron is degenerated (too flat, too long) or if the linearity assumption is wrong, these quantities do not mean much. This means that we cannot use one to validate the other. In particular, the following statement could be not true: "if the div/curl ratio is low, it means that the estimate of J is good" . Indeed, if the estimate of the divergence is wrong, it value can be high as well as low, and therefore a low value, which can be false, does not justify that the estimate of the current density is correct.

Div(B)	Div(B)/curl(B)	Curl(B)
Low	Low	Valid or not.
High	High	certainly wrong

Table 3. information given by div (B)

However, a high value means that the calculation is wrong, and therefore the estimate of J is probably wrong too. *So the value of the divergence can tell us if the current density estimate is wrong, but it cannot tell us when it is true.* (see table 3).

Thus, the errors on curl and div are not correlated on a case-by-case basis. Only the examination of a large number of cases, taken under the same conditions, can give us a valid statistical evaluation of the divergence, which can then be taken as a criterion of validity of the curl (Robert, Dunlop, et al., 1998).

Another indication on the linearity assumption is to look at the size of the tetrahedron, because we implicitly know that the larger it is, the greater the linearization errors will be. However a characteristic quantity is missing to define a critical size.

The whole problem therefore lies in the fact of knowing whether the estimate of these quantities is correct or not.

As it is difficult to know if the assumption of linearity is good or not, there remains nevertheless the consideration on the shape of the tetrahedron.

We know that if the tetrahedron is degenerated, the estimation of these quantities is false (Robert & Roux, 1990, 1993; Robert, Roux, et al., 1998; Robert, Dunlop, et al., 1998). With that, we can put a criterion on this point. After various tests, it seems that for an elongation and a planarity greater than 0.6, the estimation of the rotational and the divergence can be seriously questioned. Beyond 9, it is absolutely false.

This is why in the rest of this study, we systematically reject all the estimates of curl and div for which E or P are not less than 0.6.

Of course, with this very restrictive criterion, we loose a lot of data, butlooking at the results, the estimate of the divergence is still low. If this estimate were false, it would have taken different values depending on the regions or the time considered. However, it is weak and stable. We can therefore suggest that the estimate of the current density is not so bad.

3 Observation of Magnetic Field and Currents in Meridian Plane

3.1 Direction and Magnitude of Magnetic Field

We use the 4 GB XZ.dat file mentioned in section 2.3 to draw a map of the average magnetic field direction in the meridian plane, for a given dipole tilt angle θ. The result for $\theta = 0$ is shown figure 2. The arrows indicate the direction of the field. When the Y component of B becomes high, their length decreases. The spatial resolution for the average B is 1 R_E, while time averaging is 19 years.

Superimposed on this map, the magnetic field lines of the T87s tsyganenko model have been drawn, as well as a magnetopause calculation (last closed field line from the Earth), and finally the bow shock (Burke, 1993).

At first glance, the direction of the field is in agreement with the model, and remains in the X-Z plane as long as we are inside the magnetosphere. Beyond the bow shock, the direction becomes variable. Note that the cluster dataset is included as part of the semiempirical Tyganenko model (for last version).

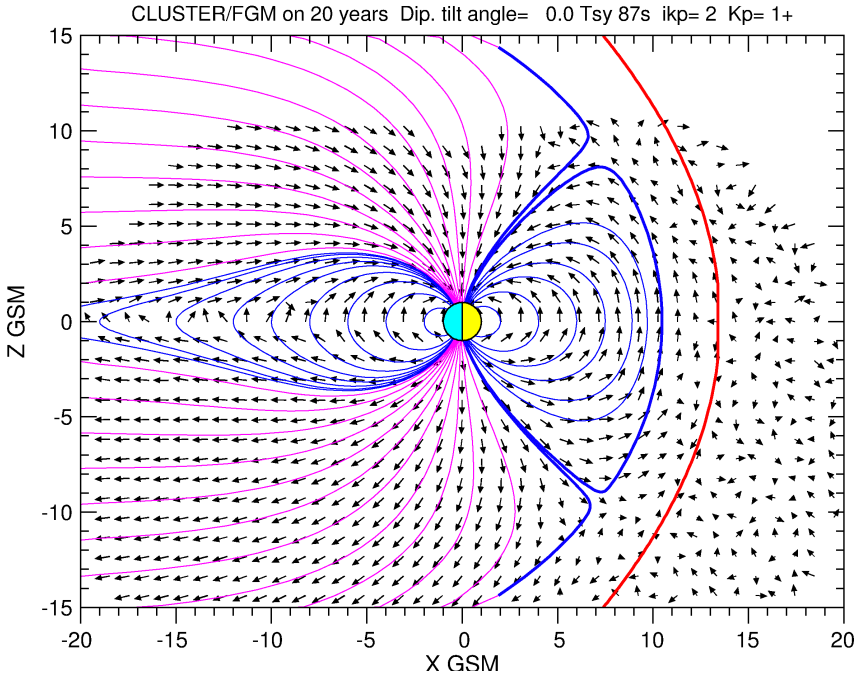

Figure 2. Average of the direction of CLUSTER/FGM magnetic field over 20 years in X-Z GSM plane, for a dipole tilt angle in [-5,5] degree range.

In figure 3 we show two other examples for $\theta \simeq +20$ and -20. The features are similar. .

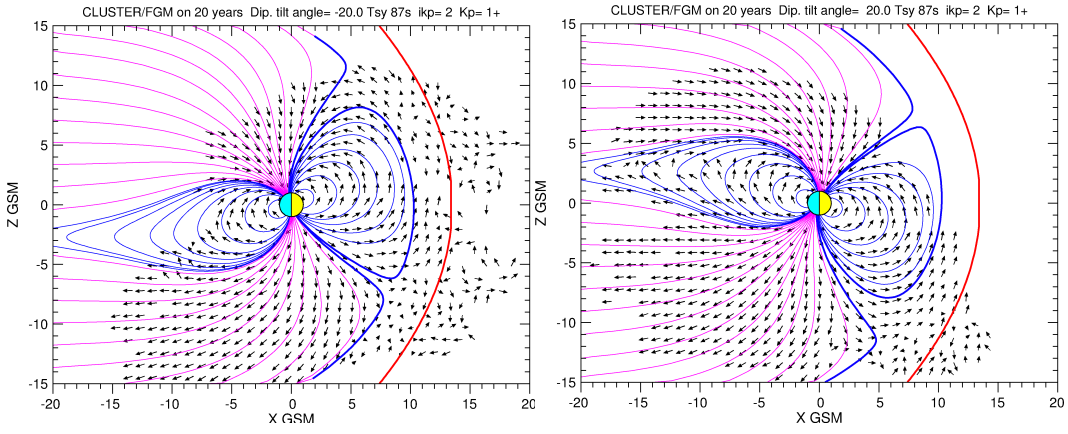

Figure 3. Same as fig.2 but with a dipole tilt angle in [-25,-15] range (left) and [15,25] (right).

Under the same conditions, figure 4, left panel, shows the map of the observed mean intensities of the magnetic field, whichcab be compared to that of T87s tsyganenko mode, on right panel.

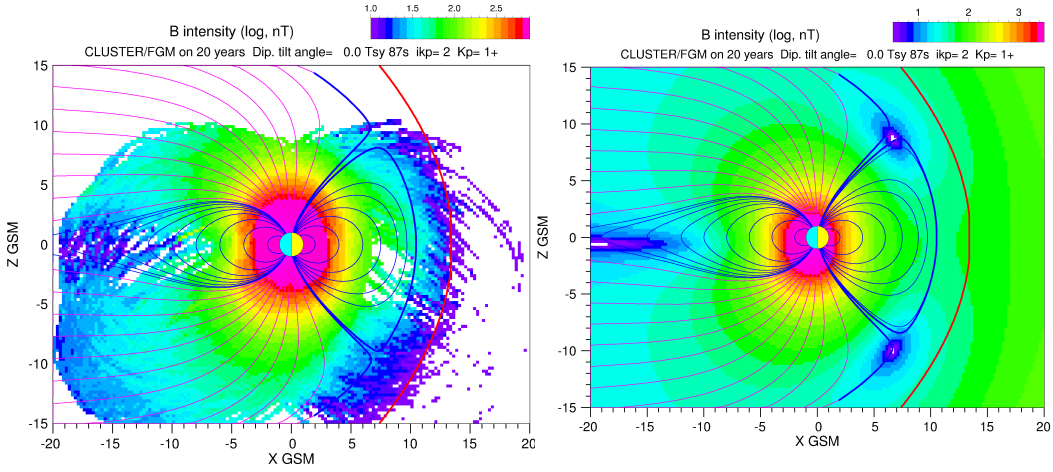

Figure 4. Average of the magnitude of CLUSTER/FGM magnetic field over 20 years in X-Z GSM plane, for a dipole tilt angle in [-5,5] degree range (left). Comparison with the magnitude deduced from Tsyganenko 87s model (right).

Near the Earth and in the tail, the fields observed are similar to those of the model: hight intensity near the Earth, weak in the tail. On the other hand, on experimental data, one does not observe very marked neutral points near the cusps, as in Tsyganenko model, and the intensity of the field decreases sharply in the cusps and beyond the magnetopause.

3.2 Direction and Magnitude of Current Density

From the previous XZ.dat file we therefore extracted all the values which respect the condition $E < 0.6$ and $P < 0.6$.

All these values are then averaged in a grid in the X-Z plane, with a resolution of 1 R_E. The intensity found is then retransmitted according to a conventional color code. Results are shown on figure 5. On the left panel, we can see a strong intensity of the currents near the cusps, rather directed towards Y. On the right panel where the Jy component has been represented, we can observe the annular current in the tail, and more modestly on the day side.

Despite the fact that we have selected the cases where the tetrahedron was not too deformed, we immediately question whether these estimates are correct. Looking at the div/curl ratio, figure 6, it seems that the observed values of the ring current could be true, ratio being less than 0.025. In the cusp region, ratio being ~ 0.10, the estimate of J (like that of div(B)) is probably not correct.

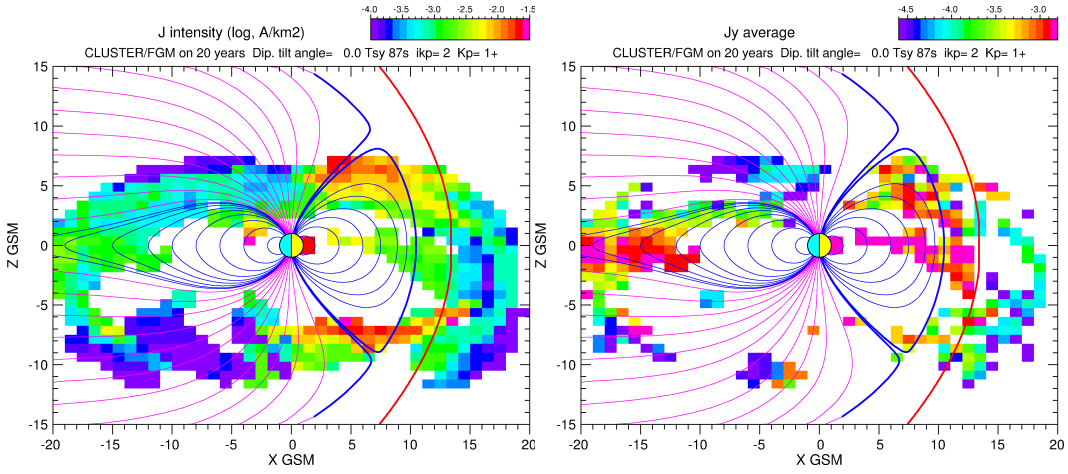

Figure 5. Magnitude of the estimated current density in the X-Z meridian plane. Left: total current, right: Jy component. Only tetrahedron with E < 0.6 and P < 0.6 have been selected.

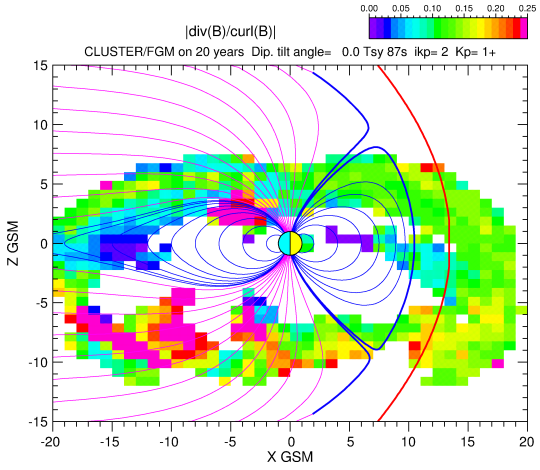

Figure 6. Magnitude of the estimated div(B) in the X-Z meridian plane.

4 Observation of Magnetic Field and Currents in Equatorial Plane

4.1 Direction and Magnitude of Magnetic Field

On Figure 7 we can see the magnetic field direction in the X-Y plane of system (left panel) and the intensity (right panel).

As we can imagine, the field is radial in this plane, as long as we stay inside the magnetosphere, and becomes anything in the magnetosheath and beyond the bow shock.

For the intensity, as expected, it decreases like a dipole, with a sudden drop beyond the bow shock.

4.2 Direction and Magnitude of Current Density

On figure 8 we can see the direction of the current in the X-Y plane of GSM system (left panel) and the intensity of the Jy component (right panel). Components Jx and Jy are not represented, but are low by respect to Jy.

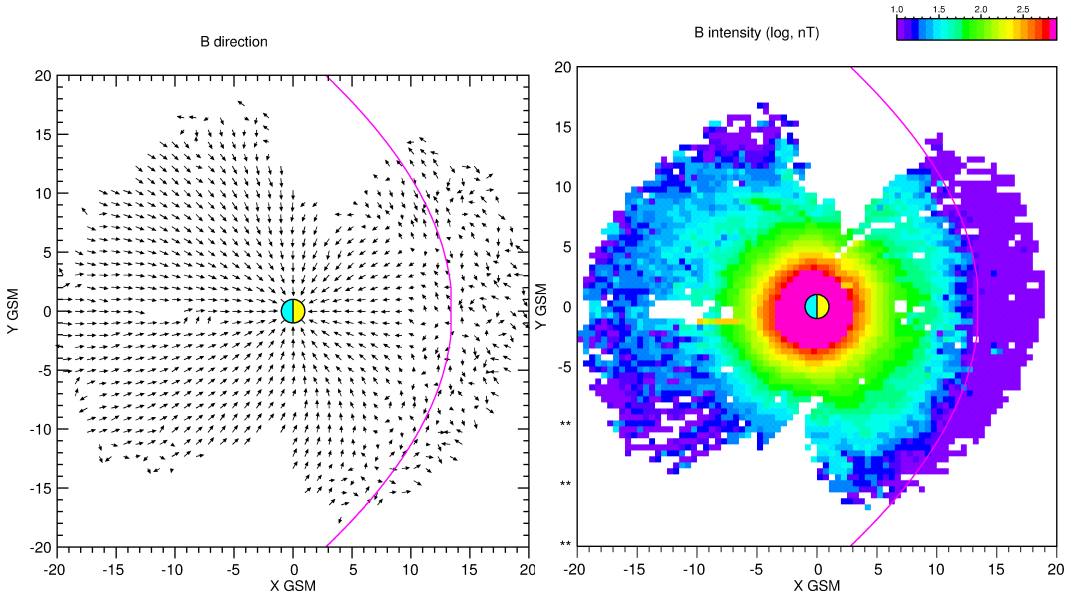

Figure 7. Direction (left) and magnitude (right) of the magnetic field in equatorial plane.

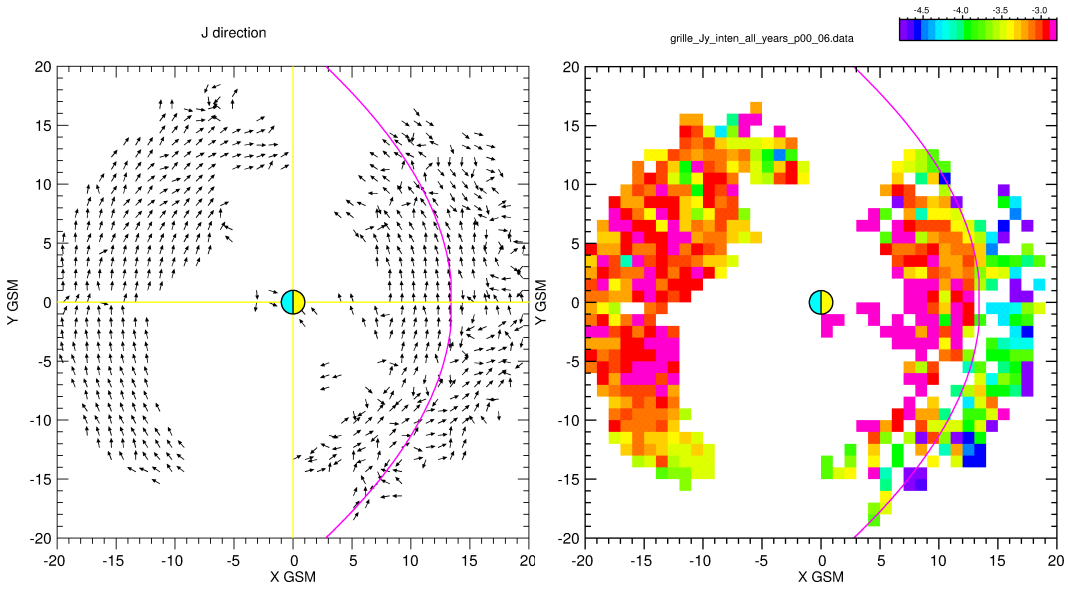

Figure 8. Direction and Magnitude of $\vec{J}$ in the Equatorial Plane. Left: direction, right: Jy

The ring current is clearly visible, and the div/curl ratio, visible on figure 9, suggests that its estimate is not false, at least on the night side (see also Zhang et al., 2011).

5 Observation of Magnetic Field and Currents in the Tail

From the YZ17.dat file mentionned in section 2.3, we therefore extracted all the values which respect the condition $E < 0.6$ and $P < 0.6$. All these values are then averaged in a grid in the X-Z plane, with a resolution of 1 Re. The $\vec{J}$ direction is shown in left panel of figure 10, while the J_y intensity is given on the right panel.

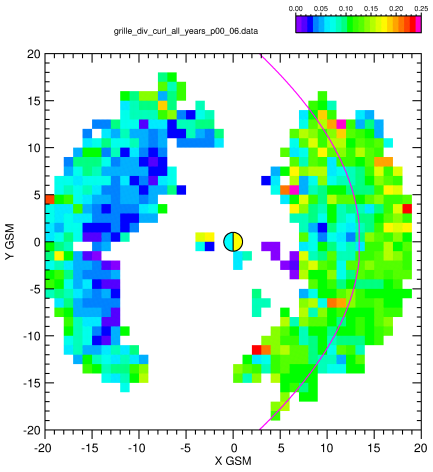

Figure 9. Div/Curl ratio for E,L < 0.6

Both results are consistent. In addition, it was verified that the component J_x was weak. We can clearly see again the ring current. Nevertheless it should be noted that apart from the strong values (in red), located between $z = \pm 3$, the div/curl ratio becomes high, particularly for $-8 < z < -3$.

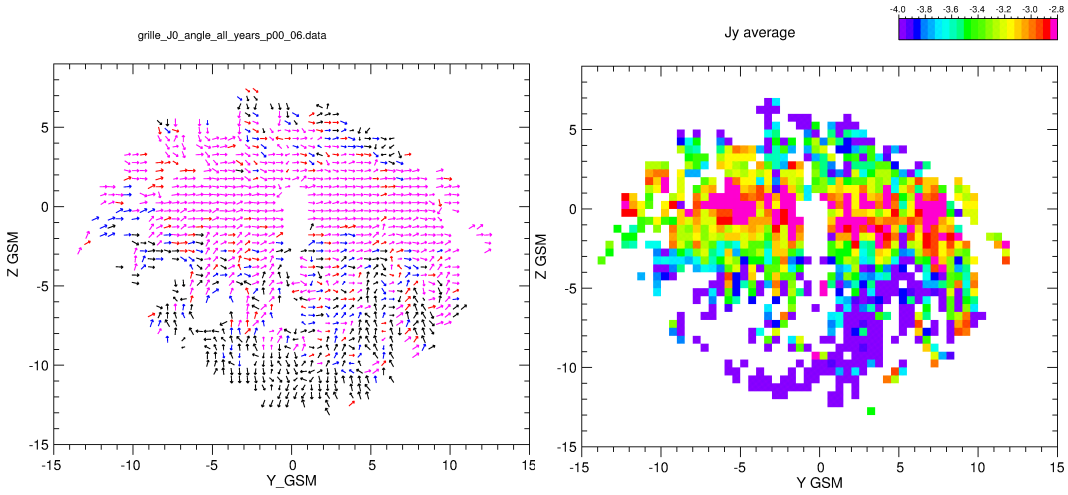

Figure 10. Direction of the current (left panel) and intensity of the J_y component in a Y-Z plane located at x=-17 R_E

6 Towards a Simplified Day-side Magnetopause Model

6.1 Experimental Results

The observation of the direction of $\vec{B}$ in the meridian and equatorial planes, for a fixed value of the dipole tilt angle, and for values averaged over twenty years, shows a very good organization of the field inside the magnetosphere. On the other hand, as soon as we cross the magnetopause, or even more after the bow shock, the direction of the field

becomes disorganized. Hence, we propose the idea of using these field maps to define a magnetopause model, essentially on the day side, where we have enough data.

We have therefore recalculated the mean direction of $\vec{B}$ in these two planes, but with a greater resolution ($0.5R_E$). Results are shown in fig. 11.

For the meridian plane, the magnetopause could be simulated by a half ellipsoid, with major axis along X and minor axis along Z. The characteristics of which are given below:

Center: **(-8.2, 0, 0)** Semi major axis : **20.1** Semi minor axis : **16.9**

Figure 11 shows that this very simple model applies quite well to the average experimental data. We have verified that it also provides good results when the dipole tilt angle changes, up to plus or minus 30 degrees.

Field lines are drawn by hand, using the direction of the field.

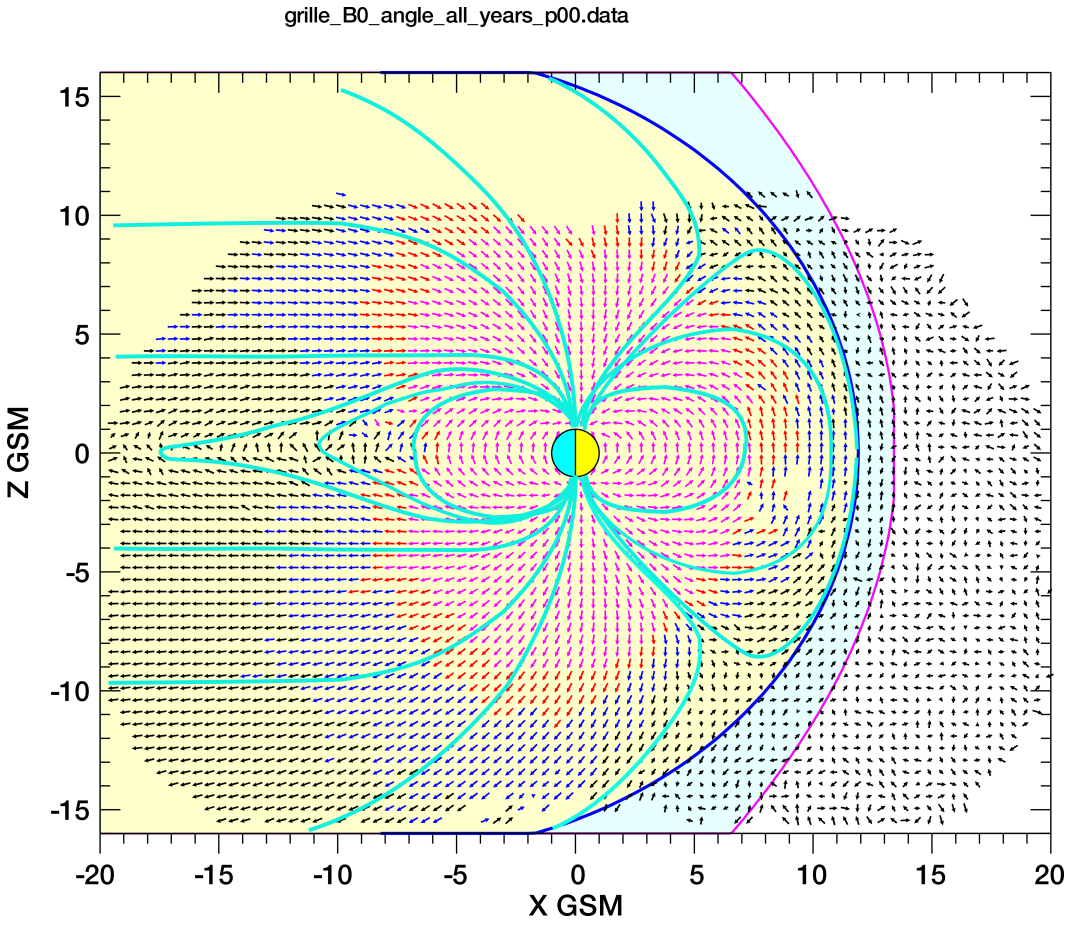

Figure 11. Hight Resolution Average of the direction of CLUSTER/FGM magnetic field over 20 years in X-Z GSM plane, for a dipole tilt angle in [-5,5] degree range.Magnetopause, cusps and some field lines are plotted from the observed mean values of the direction of the magnetic field.

A similar graph was made in the equatorial plane, as well as in the Y-Z plane, in order to determine the magnetopause in 3 dimensions, in particular the c (towards Y) axis of the ellipsoid (see fig. 12). There again, we could approximate the magnetopause

by a half ellipse with the same center as previously, and defined by its 3 axes a, b, c. We thus have a simple model with the following characteristics:

Center O : **(-8.2, 0, 0)** a= **20.1** b= **16.9** c= **18.**

The magnetopause model shows the boundary between field lines having a defined geometry (here radial) and the part of space where they appear to be disorganized. We can therefore conclude that the model is acceptable.

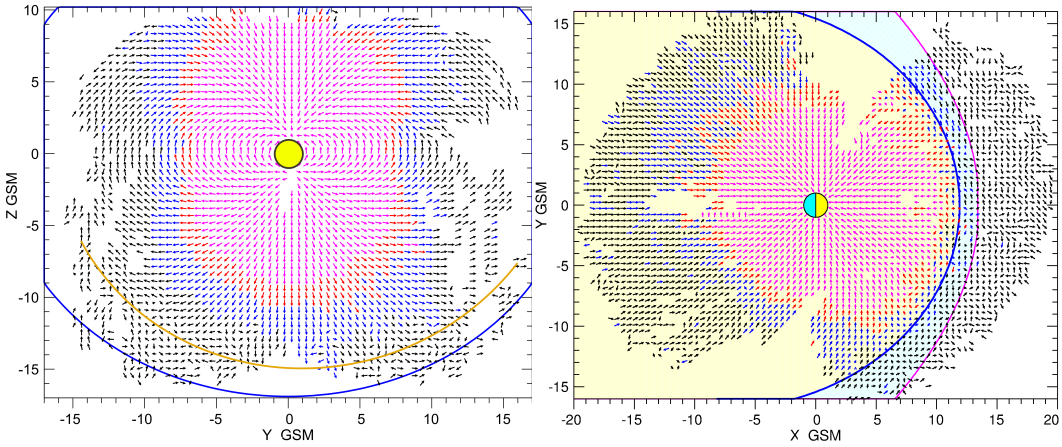

Figure 12. Hight Resolution Average of the direction of CLUSTER/FGM magnetic field over 20 years, for a dipole tilt angle in [-5,5] degree range. Left panel: YZ plane in GSM, right: XY plane

6.2 Model and Equation

For the magnetopause plot, the following classic formulas are used. Angles α and β can be viewed as a latitude and a longitude for a coordinate system centered on the point O.

$$x = O_x + a\cos\alpha \qquad y = c\sin\beta \qquad z = b\sin\alpha$$

with $-\pi/2 < \alpha < \pi/2 \qquad -\pi/2 < L < \pi/2$

On the night side, having no data available, we are content to slightly extend this magnetopause by a cylinder of elliptical section, tengent at the summits of the ellipsoid.

6.3 Cusps Position in the XZ Meridien Plane

Figure 13 shows the direction of the field in the XZ plane for different values of the angle of the dipole.

On each panel, we tried to determine the limit separating the internal field of the magnetosphere, ie the horn itself. We thus have an approximation of the latitude of the cusps as a function of the dipole tilt angle. Results are shown in table 4.

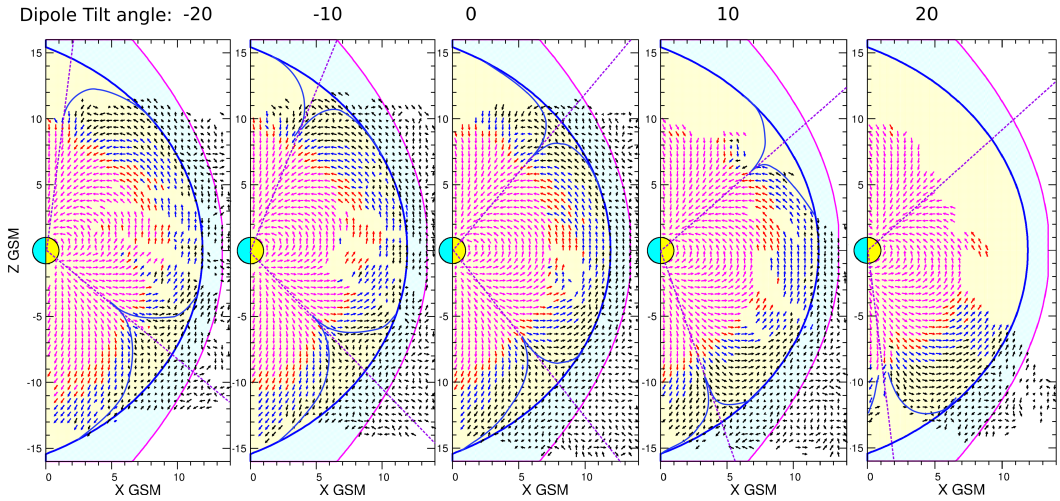

Figure 13. Cusps position and shape in XZ GSM plane pour various values of dipole tilt angle.

	Dipole Tilt Angle	-20	-10	0	10	20
North cusp	Latitude	82	68	50	∼42	∼42
South cusp	Latitude	42	48	52	71	∼83

Table 4. Cusps Position in GSM

7 Observation of Magnetic Field and Currents near the Cusps

7.1 Definition of CDM Coordinate System

To investigate the topology of the lines strengh near the cusp is introduced the CDM system, defined figure 14. We model the magnetopause around the cusp by a sphere of radius R and a center positioned at O. The $\vec{C}$ axis is perpendicular to the surface of the sphere, the axis $\vec{M}$ is tengeant north, and finally the axis $\vec{D}$ is tengeant to the dusk. In fact, for studies around cusps, a single sphere correctly approximates the ellipsoid described in section 6., and is easier to use.

Note that the geometry of magnetic field lines has already been discussed by Shen et al. (2008) and in the review by Shen and Dunlop (2008).

Otherwise the angle α and β can be viewed as a latitude and a longitude for a coordinate system centered on the point O.

In this section, we took (in R_e) $O_x = -3.4, O_y = 0, O_z = 0$, and $R = 15$ and we selected all points below R until $10R_E$. Thus we select the points inside the cusp, without going beyond the magnetopause.

7.2 GSM to CDM Transformation

The direction of any vector $\vec{V}$ in GSM is tranformed in CDM by the formula:

$$\begin{aligned} W_C &= (V_x - 0_x)\cos\alpha\cos\beta + V_y\cos\alpha\sin\beta + V_z\sin\alpha \\ W_D &= -(V_x - 0_x)\sin\beta + V_y\cos\beta \\ W_M &= -(V_x - 0_x)\sin\alpha\cos\beta - V_y\sin\alpha\sin\beta + V_z\cos\alpha \end{aligned}$$

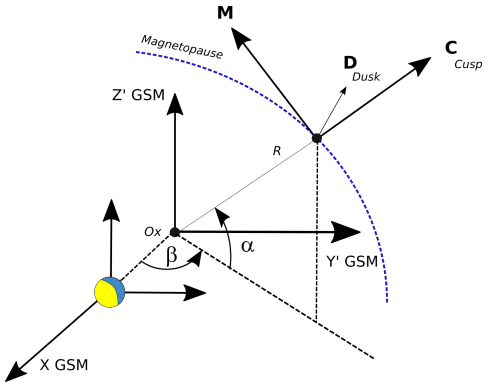

Figure 14. Definition of CDM Coordinate System.

7.3 Direction of Magnetic Field in CDM Coordinates

7.3.1 Size and Position of the Cusps

Figure 15 shows the direction of the magnetic field in the CDM frame, ie at the surface of the sphere defined in section 7.1.The length of the arrows corresponds to the projection on the surface of the sphere, a non-zero orthogonal component will produce a shorter arrow. Colors vary with the intensity of the field (in the direction from yellow, cyan, blue, red to magenta). On the left panel the calculations were made for a dipole tilt angle θ equal to zero. On the right panel θ was taken at -20 degrees. The cusps are distinguished by the change in direction of the field at the edge, on the surface of the magnetopause. Because of the distribution of the available data, the southern cusp is better defined. It is not resolved in the data for $\theta = -20$.

In fact, the detection of the contour of the cusp is not evident, because the field lines are strongly disturbed, in particular inside the horn. We find roughly the same latitude as the one estimated in section 6.3, but the shape itself of the polar horn is not obvious, and its position in longitude not exactly in front of the sun (at zero longitude).

Of course the image is distorted, because, as for a world map, the projection of the surface of a sphere on a plane expands the poles. Nevertheless one could distinguish for the south cusp, better defined, one or two species of "secondary cusps" not very well defined. For the south cusp, we tried another type of projection, which appreciates distances better, by placing itself in a tengent plane at the magnetopause, just above the cusp. The results can be seen in figure 16 . For $\theta = 0$, the main cusp is better defined, and we could see, instead of two cusps, a single cusp but of rather odd shape. Therefore the shape, position and extent of the cusp is not clearly defined in longitude, while it is in latitude. There are then two possibilities:

- either the position and the shape of the cusp, in longitude, do not depend only on the dipole tilt angle, but also, which is probable, on other factors such as the pressure of the solar wind or other, and the fact of averaging the data over several years leads to a fanciful result,

-or the shape of the cusp is not a simple funnel as in the artist's views, but in fact something more complicated and not stable in the GSM coordinate system.

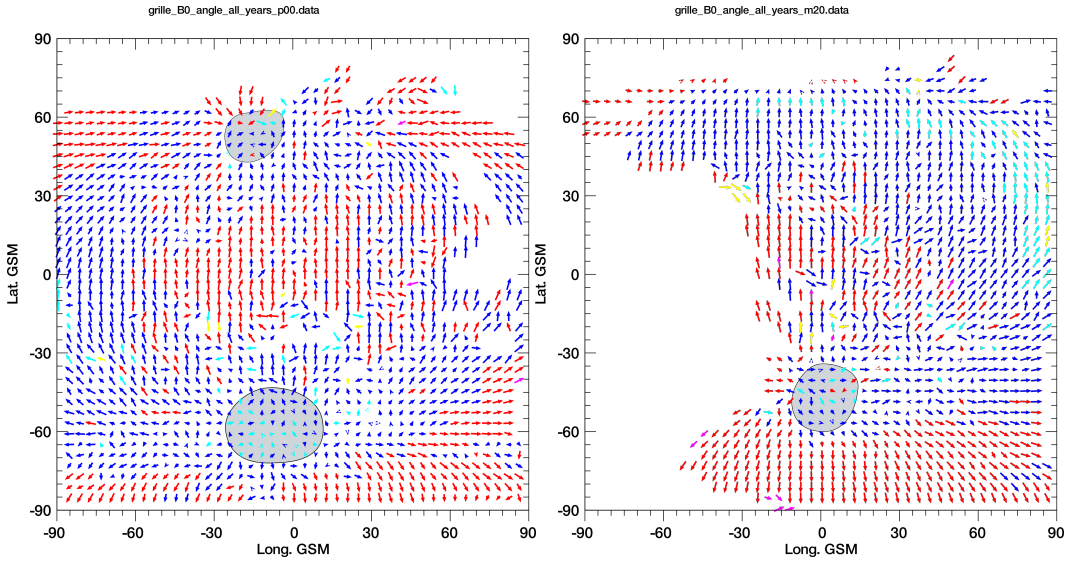

Figure 15. Direction of the magnetic field at the surface of the sphere modeling the magnetopause. Left: dipole tilt angle=0; right: -20 degrees.

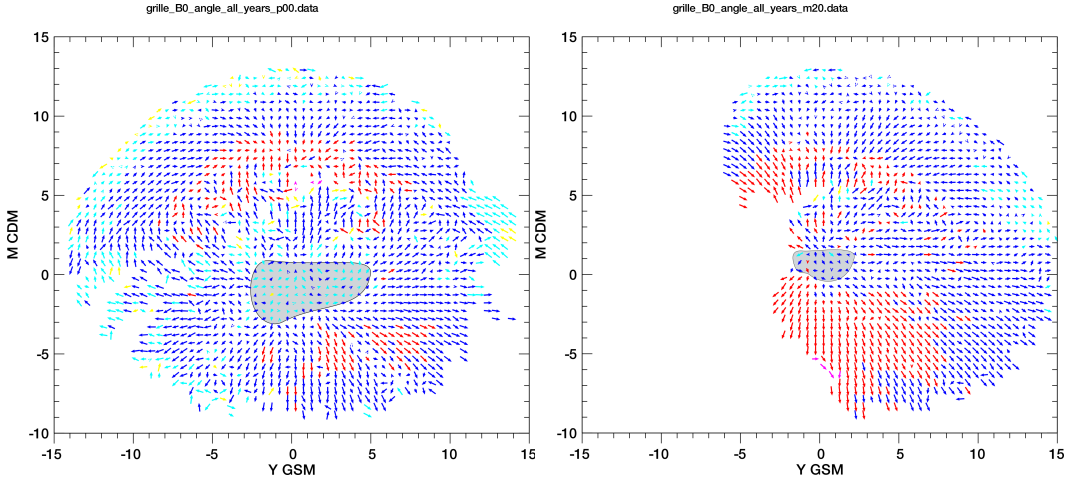

Figure 16. Direction of the magnetic field at the surface of the sphere modeling the magnetopause. Left: dipole tilt angle=0; right: -20 degrees.

7.4 Magnitude of Current Density in CDM Coordinates

Fig 17 shows the intensity of the current (left panel) and the div/curl ratio (right panel), for an elongation and a planarity of less than 0.6.

The div/curl ratio is not negligible (between 0.10 and 0.15) and one can ask the question of the validity of the estimate of $\vec{J}$. Nevertheless, it seems realistic to think that there are currents in this region.

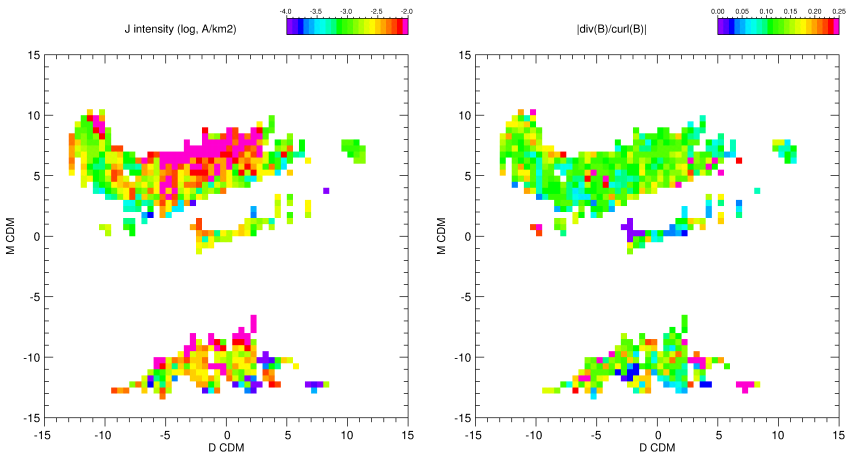

Figure 17. Current Density (left) and Div/Curl ratio (right) for $E < 0.6 and P < 0.6$.

8 Towards a Digital Model of a Magnetospheric Magnetic Field

8.1 General Remarks

All of the previous figures show the use of average data and the results can be considered as tests of the validity of this data set. However, all graphics are in a 2D plane, but the dataset covers a spatial volume. As for the magnetopause model, we therefore propose the idea of a digital magnetic field model, capable of giving a value of $\vec{B}$ at any point in the space covered by the data. This model is based on the average data in a 3D grid, and the value of $\vec{B}$ at any point inside an elementary cell can be found by spatial interpolation.

8.2 Size and Spatial Resolution

We therefore have the average values of the magnetic field in a 3-D grid of about $40R_E$ with a resolution of 0.2 to $1R_E$ ($\sim$ 1000 to 6000 km). Of course, the higher the resolution is, the more empty cells will be. However, from the files defined in section 2.3, we can create an arbitrary resolution grid depending on what we want to do.

With this data grid, we can, inside each elementary cell, do a 3-D interpollation in order to have a field value at any point in space.

We therefore have access to a field model derived only from the experimental measurements of fields, averaged over 20 years, and only depend of the dipole tilt angle. This model is worth what it is worth, but has the advantage of being simple, not theoretical, and able to describe the average behavior of the field on a large scale.

8.3 Spatial Interpolation

Figure 18 shows the elementary cube in which we will calculate the field at point M by spatial interpolation of the eight field values at the top of the eight vertices of the cube.

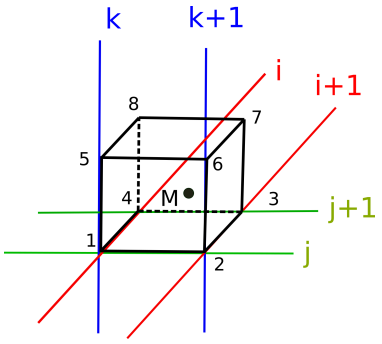

Figure 18. Spatial interpolation of a point inside cell.

Each point inside the 3-D grid is in an elementary cell, defined by the position of its eight vertices by:

$$P1 = \begin{pmatrix} P_i \\ P_j \\ P_k \end{pmatrix} \quad P2 = \begin{pmatrix} P_i \\ P_{j+1} \\ P_k \end{pmatrix} \quad P3 = \begin{pmatrix} P_{i+1} \\ P_{j+1} \\ P_k \end{pmatrix} \quad P4 = \begin{pmatrix} P_{i+1} \\ P_j \\ P_k \end{pmatrix}$$

$$P5 = \begin{pmatrix} P_i \\ P_j \\ P_{k+1} \end{pmatrix} \quad P6 = \begin{pmatrix} P_i \\ P_{j+1} \\ P_{k+1} \end{pmatrix} \quad P7 = \begin{pmatrix} P_{i+1} \\ P_{j+1} \\ P_{k+1} \end{pmatrix} \quad P8 = \begin{pmatrix} P_{i+1} \\ P_j \\ P_{k+1} \end{pmatrix}$$

As for the positions, we define the values of the field at the eight vertices of the cube by:

$$B1 = \begin{pmatrix} B_i \\ B_j \\ B_k \end{pmatrix} \quad B2 = \begin{pmatrix} B_i \\ B_{j+1} \\ B_k \end{pmatrix} \quad B3 = \begin{pmatrix} B_{i+1} \\ B_{j+1} \\ B_k \end{pmatrix} \quad B4 = \begin{pmatrix} B_{i+1} \\ B_j \\ B_k \end{pmatrix}$$

$$B5 = \begin{pmatrix} B_i \\ B_j \\ B_{k+1} \end{pmatrix} \quad B6 = \begin{pmatrix} B_i \\ B_{j+1} \\ B_{k+1} \end{pmatrix} \quad B7 = \begin{pmatrix} B_{i+1} \\ B_{j+1} \\ B_{k+1} \end{pmatrix} \quad B8 = \begin{pmatrix} B_{i+1} \\ B_j \\ B_{k+1} \end{pmatrix}$$

We calculate the distance from point M to each vertex by:

$$d1 = \left[(M_x - P1_x)^2 + (M_y - P1_y)^2 + (M_z - P1_z)^2)\right]^{1/2}$$
$$\cdots$$
$$d8 = \left[(M_x - P8_x)^2 + (M_y - P8_y)^2 + (M_z - P8_z)^2\right]^{1/2}$$

Each value of B is assigned a weight equal to the inverse of its distance from M:

$$W_n = \frac{1}{dn}$$

And we calculate the field at point M by the weighted average of the field at each vertex of the cube:

$$B_x = \frac{\sum_{n=1}^{8} Bn_x W_n}{\sum_{n=1}^{8} W_n} \qquad B_y = \frac{\sum_{n=1}^{8} Bn_y W_n}{\sum_{n=1}^{8} W_n} \qquad B_z = \frac{\sum_{n=1}^{8} Bn_z W_n}{\sum_{n=1}^{8} W_n}$$

Thus we can continuously obtain the value of the field at any point located inside the 3-D grid. Of course, the higher the resolution of the grid, the better the precision.

High resolution will have a lot of empty cells, because CLUSTER's trajectory does not go through all points in space, even averaging over twenty years. Conversely, a low resolution will ensure that each cell will be calculated from a large number of measurement points.

Then, a 40x40x40 grid on a spatial dimension of 40 R_E will be almost full (except at the edges), but the elementary cubes will be large: $1R_E$.

In the case of a high resolution, the 6 vertices of the cubes are therefore very likely not to all have a value of $\vec{B}$. An interesting option is then, in case of absence of data at this scale, is to allow to interpolate in a larger cube, of dimension 3x3x3 of the elementary cube, this one being then in the center of a larger cube. Of course, the weights associated with these values will always be inversely proportional to the distance from the point where we want to calculate the field. But in case the elementary cube has enough values of $\vec{B}$, the high resolution is preserved. Otherwise, we degrade the resolution, but we increase the possibility of having a measurement point.

This otion has been used in the following examples, based on an elementary cube of 0.5 R_E.

8.4 Application to Field Line Drawing

8.4.1 Field Line in Meridian Plane

As we can calculate the field at any point in space, we can therefore apply a ray tracing program, like the TRACE subroutine in Tsyganenko's model (Tsyganenko, 1987). Starting from a point in the space of the grid, we thus calculate all the points of a magnetic field line.

This is what we did in figure 19, in the meridian plane.

Of course, the lines are not complete, because the grid has a lot of empty cells, but we still get an overview of the field lines inside the magnetosphere.

We can compare the shape of the field lines, deduced from the expérimental model, to those drawn by hand in figure 11.

It is unfortunate that the zones of the north cusp are not better defined, because of the empty cells, but nevertheless the general appearance of the field lines obtained is quite plausible. The fluctuations visible in the queue are probably due to the 20 year averaging of the data. Note that on the day side, the limit of the closed field lines coincides well with the average magnetopause model proposed in section 6.

Beyond the magnetopause, the field lines get a little anything.

Figure 20 shows two orther examples of field line tracing in the meridian plane, for dipole tilt angle = -20 (left) and +20 (right). For $\theta = -20$, the data gris does not contains many points, but enough to show the limit of the magnetopause, and the south cusp. For $\theta = +20$, the two cusps are well defined. However, it would seem that for these examples, the magnetopause is a little closer than predicted by the model.

8.4.2 Field Line Near the Cusps

To visualize the field lines near the cusps, we place ourselves in the CMD coordinate system defined in section 7.1, for a latitude that we estimated in section 6.3, table 4. We are in a plane perpendicular to the direction of the Earth, therefore practically tengent to the magnetopause, and at a distance slightly less (8 R_E). The center of the CMD system is assumed to be the center of the cusp. In this plane, we start the field

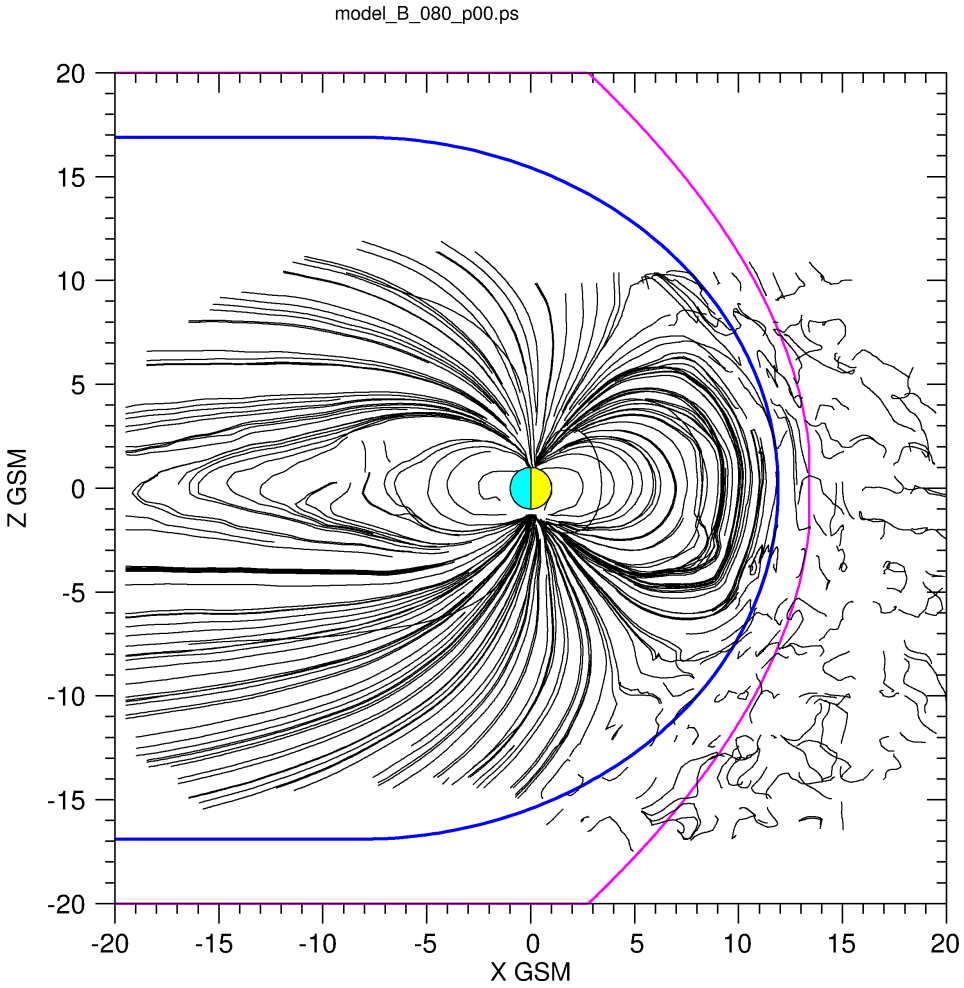

Figure 19. Field Line Tracing from Digital Magnetic Field Model build from averaged data, for a dipole tilt angle $\theta = 0$

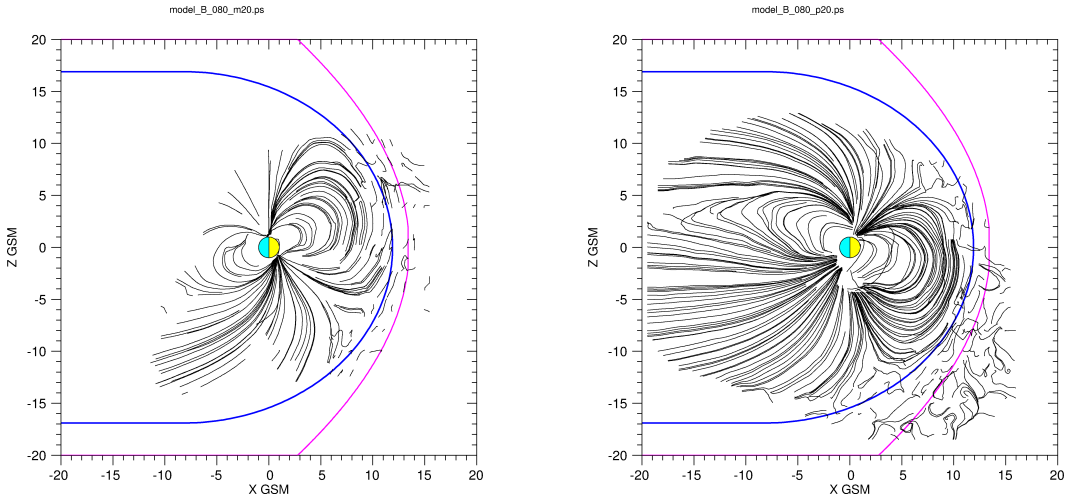

Figure 20. Same as Fig. 19but for $\theta = -20$ (left) and $\theta = +20$ (right)

lines computation from a series of points following a circle of radius 3 R_E. The field lines are calculated in both directions, parallel and anti-parallel to $\vec{B}$.

The results are shown in Figures 21 and 22, for the North and South cusps, and for various dipole tilt angle. The cone shape of the cusps is easily recognizable, although the field lines are disturbed. One can compare figure 20 with figure 15 of section 7.3.1, where the cusps had been identified with the map of the directions of the field. There is indeed only one cornet, the shape of which is irregular, but well defined.

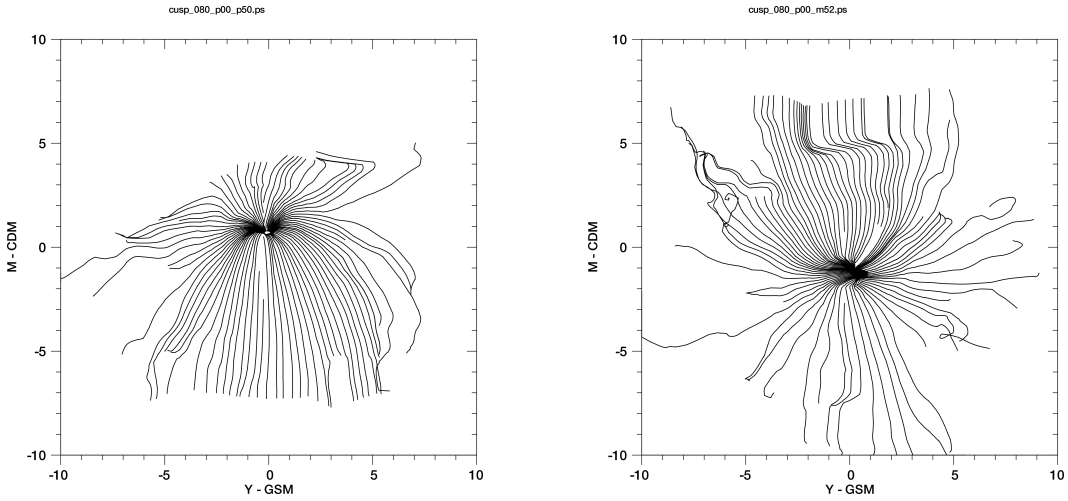

Figure 21. Field Line Tracing from Numerical Magnetic Field Model near the north cusp (left) and the south cusp (right) for a dipole tilt angle $\theta = 0$.

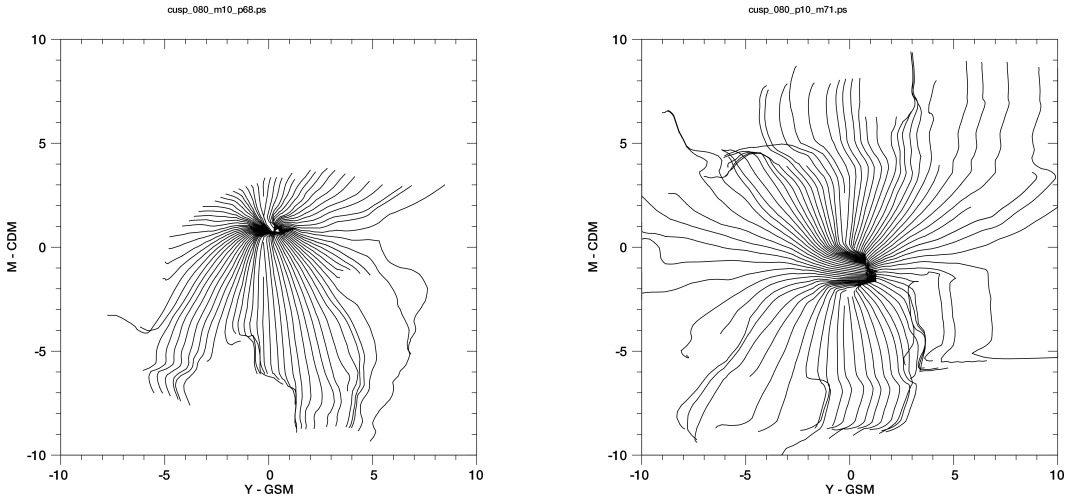

Figure 22. Field Line Tracing from Numerical Magnetic Field Model near the north cusp (left) for $\theta = -10$ and the south cusp (right) for $\theta = 10$

8.4.3 Cusps Field Line in the YZ plane

It can be interesting to calculate the field lines near the cusps, in the Y-M frame, and to project the result in the YZ plane of the GSM, in order to have a view of the front face of the magnetosphere.

This is what can be seen in figure 23. As the field lines are calculated near each cusp, the lines are not all connected near the equator. As for a planisphere, this projection enlarges the Y dimension. This figure is a 3-D projection, the field lines located inside the horn are masked by those in the front.

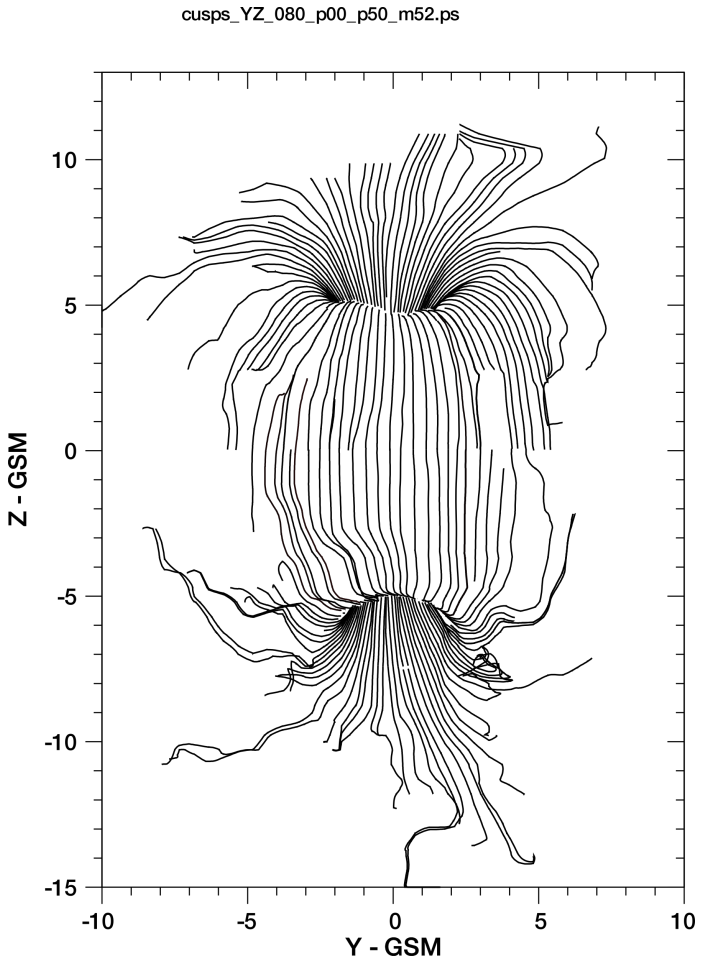

Figure 23. Projection in YZ plane of Field Line Tracing computed near each cusp ($\theta = 0$).

9 Conclusions

The use of twenty years of data of the FGM magnetometer made it possible to study the average behavior of the magnetic field, according to the values of the dipole tilt angle.

Creation of a magnetic field database where all $\vec{B}$ vectors and all positions of the 4 spacecraft are time aligned made it possible to calculate curl and div of $\vec{B}$ over the entire duration of the mission, and made it possible to produce current density maps, in addition to those of the magnetic field. The validity of the estimate of this density has

been discussed, but not really decided, and it is likely that the question will remain open for a long time. Maybe note that MMS allows comparison to plasma currents(Dunlop et al., 2018).

A field average 3-D data grid was calculated, and is available year by year, or averaged over twenty years, and can be used for other studies. It leads to a numerical model of the average field, as well as to a simple model of magnetopause.

Numerical magnetic field model, based on this grid containing experimental averaged values of the magnetic field, provides a value of the field in any point (if the grid is full) and makes it possible to calculate field lines.

Therefore, position and shape of the cusp have been studied, not only in latitude, but also in longitude.

The possibility of adding data from other missions (THEMIS, MMS) to this grid would make it possible to obtain better spatial coverage, and therefore maps of direction and intensity more extensive in space, notably on the night side. This addition would also make it possible to fill a lot of empty cells in the grid, and to obtain more precise field line maps. Other indicators, in addition to the dipole tilt angle, could be added (magnetic indices, solar wind parameters).

In a future work it would be interesting to compare this field line model with the Magnetic field Rotation Analysis method (MRA) developped by Shen et al. (2007), and comparisons to MHD models.

Acknowledgments

The author is deeply grateful to the entire FGM team, past and present, for their ongoing efforts over more than 20 years to building a magnificent collection of magnetic field data over all these years. This work is supported by STFC in-house research grant ST/M001083/1, NSFC grants 41821003 and 41874193.

It is also thanks to the efforts of ESA's Cluster Science Archive (Laakso et al., 2010) that these data are now public (see `https://www.cosmos.esa.int/web/csa/access`), and their ease of access and download is remarkable and commendable .

References

Allen, A., Schwartz, S., Harvey, C., Perry, C., Huc, C., & Robert, P. (2004, apr 16). *Csds archive task group, "cluster exchange format, data file syntax", ds-qmw-tn-0010,issue 2 rev. 0, issue 2 rev. 0* (Tech. Rep.). ESA.

Balogh, A., Cowley, S. H., Dunlop, M., Southwood, D., Thomlinson, J., Glassmeier, K.-H., ... Tsurutani, B. (1993). The Cluster Magnetic Field Investigation: Scientific Objectives and Instrumentation. In R. Schmidt (Ed.), *Cluster: Mission, Payload and Supporting Activities* (p. 95-114). Paris, France: European Space Agency.

Balogh, A., Dunlop, M., Cowley, S. H., Southwood, D., Thomlinson, J., Glassmeier, K.-H., ... Kivelson, M. (1997). The Cluster magnetic field investigation. *Space Science Reviews*, *79*, 65-91.

Burke, W. (1993, March). Cluster : mission, payload, and supporting activities. In (p. 264).

Chanteur, G. (1998, July). Spatial interpolation fo four spacecraft: Theory. In G. Paschman & P. Daly (Eds.), *Analysis Methods for Multi-Spacecraft Data* (p. 349-369). European Space Agency.

Chanteur, G., & Harvey, C. (1998, July). Spatial interpolation fo four spacecraft: Application to magnetic gradients. In G. Paschman & P. Daly (Eds.), *Analysis*

Methods for Multi-Spacecraft Data (p. 371-393). European Space Agency.

Chanteur, G., & Mottez, F. (1993). Geometrical tools for Cluster data analysis. In *Proc. international conf. "spatio-temporal analysis for resolving plasma turbulence (start)", aussois, 31 jan. 31–5 feb. 1993* (p. 341-344). Paris, France: European Space Agency.

Dunlop, M., Balogh, A., Southwood, D., Elphic, R. C., Glassmeier, K.-H., & Neubauer, F. M. (1990, May). Configurational sensitivity of multipoint magnetic field measurements. In E. Rolfe (Ed.), *Proceedings of the international workshop on "space plasma physics investigations by cluster and regatta", graz, feb. 20–22,1990* (p. 20-22). Paris, France: European Space Agency.

Dunlop, M., Southwood, D., Glassmeier, K.-H., & Neubauer, F. (1988). Analysis of multipoint magnetometer data. *aisr*, *8*, (9)273-(9)277.

Dunlop, M. W., Balogh, A., Glassmeier, K.-H., & Robert, P. (2002). Four-point cluster application of magnetic field analysis tools: The curlometer. *Journal of Geophysical Research: Space Physics*, *107*(A11), SMP 23-1-SMP 23-14. Retrieved from `https://agupubs.onlinelibrary.wiley.com/doi/abs/10.1029/2001JA005088` doi: https://doi.org/10.1029/2001JA005088

Dunlop, M. W., & Eastwood, J. P. (2008, January). The Curlometer and Other Gradient Based Methods. *ISSI Scientific Reports Series*, *8*, 17-26.

Dunlop, M. W., Haaland, S., Dong, X.-C., Middleton, H. R., Escoubet, C. P., Yang, Y.-Y., ... Russell, C. T. (2018). Multipoint analysis of electric currents in geospace using the curlometer technique. In *Electric currents in geospace and beyond* (p. 67-80). American Geophysical Union (AGU). Retrieved from `https://agupubs.onlinelibrary.wiley.com/doi/abs/10.1002/9781119324522.ch4` doi: https://doi.org/10.1002/9781119324522.ch4

Dunlop, M. W., Yang, J.-Y., Yang, Y.-Y., Lühr, H., & Cao, J.-B. (2020). Multi-spacecraft current estimates at swarm. In M. W. Dunlop & H. Lühr (Eds.), *Ionospheric multi-spacecraft analysis tools: Approaches for deriving ionospheric parameters* (pp. 83–116). Cham: Springer International Publishing. Retrieved from `https://doi.org/10.1007/978-3-030-26732-2_5` doi: 10.1007/978-3-030-26732-2_5

Khurana, K., Kepko, E., Kivelson, M., & Elphic, R. (1996). Accurate determination of magnetic field gradients from four point vector measurements: Ii. use of natural constraints on vector data obtained from four spinning spacecraft. *IEEE Trans. Magn.*, *32*, 5193.

Laakso, H., Perry, C., McCaffrey, S., Herment, D., Allen, A. J., Harvey, C. C., ... Turner, R. (2010, January). Cluster Active Archive: Overview. *Astrophysics and Space Science Proceedings*, *11*, 3-37. doi: 10.1007/978-90-481-3499-1_1

Robert, P. (2011, February). *The roproc file format, a dedicated file format for vectorial data processing", version 2.2* (Tech. Rep.). Ecole Polytechnique, route de Saclay,91128 PALAISEAU CEDEX, FRANCE: CNRS/LPP. (http://cdpp.cesr.fr)

Robert, P. (2021, Avril). *The roproc commands: A set of procedures for spatial time serie data processing, version 5.1* (Tech. Rep.). Ecole Polytechnique, route de Saclay,91128 PALAISEAU CEDEX, FRANCE: LPP-ScientiDev. (http://cdpp.cesr.fr)

Robert, P., Dunlop, M., Roux, A., & Chanteur, G. (1998, July). Accuraccy of current density determination. In G. Paschman & P. Daly (Eds.), *Analysis Methods for Multi-Spacecraft Data* (p. 395-418). European Space Agency.

Robert, P., & Roux, A. (1990, may). Accuracy of the estimate of J via multipoint measurements. In E. Rolfe (Ed.), *Proceedings of the international workshop on "space plasma physics investigations by cluster and regatta", graz, feb. 20–22,1990* (p. 29-35). Paris, France: European Space Agency.

Robert, P., & Roux, A. (1993). Influence of the shape of the tetrahedron on the accuracy of the estimation of the current density. In *Proc. international conf.*

"spatio-temporal analysis for resolving plasma turbulence (start)", aussois, 31 jan. 31–5 feb. 1993 (p. 289-293). Paris, France: European Space Agency.

Robert, P., Roux, A., & Chanteur, G. (1995, July). Accuracy of the determination of the current density via four satellites. In *Abstracts.* Boulder, Colorado. (Presentation GAB51H-06)

Robert, P., Roux, A., & Coeur-Joly, O. (1995, June). Validity of the estimate of the current density along Cluster orbit with simulated magnetic data. In *Proceedings of cluster workshops, braunschweig, 28–30 sep. 1994, toulouse, 16–17 nov. 1994* (p. 229-233). Paris, France: European Space Agency.

Robert, P., Roux, A., Harvey, C., Dunlop, M., Daly, P., & Glassmeier, K.-H. (1998, July). Tetrahedron geometric factors. In G. Paschman & P. Daly (Eds.), *Analysis Methods for Multi-Spacecraft Data* (p. 323-348). European Space Agency.

Shen, C., & Dunlop, M. W. (2008, January). Geometrical Structure Analysis of the Magnetic Field. *ISSI Scientific Reports Series*, *8*, 27-32.

Shen, C., Li, X., Dunlop, M., Shi, Q. Q., Liu, Z. X., Lucek, E., & Chen, Z. Q. (2007). Magnetic field rotation analysis and the applications. *Journal of Geophysical Research: Space Physics*, *112*(A6). Retrieved from `https://agupubs.onlinelibrary.wiley.com/doi/abs/10.1029/2005JA011584` doi: https://doi.org/10.1029/2005JA011584

Shen, C., Rong, Z., Li, X., M, D., Liu, Z., Malova, H., ... C, C. (2008, 11). Magnetic configurations of tail tilted current sheet. *Annales Geophysicae*, *26*. doi: 10.5194/angeo-26-3525-2008

Thébault, E., Finlay, C. C., Beggan, C. D., Alken, P., Aubert, J., Barrois, O., ... Zvereva, T. (2015, May 27). International geomagnetic reference field: the 12th generation. *Earth, Planets and Space*, *67*(1), 79. Retrieved from `https://doi.org/10.1186/s40623-015-0228-9` doi: 10.1186/s40623-015-0228-9

Tsyganenko, N. A. (1987). Global quantitative models of the geomagnetic field in the cis-lunar magnetosphere for different disturbance levels. *pps*, *35*, 1347-1359.

Zhang, Q.-H., Dunlop, M., Lockwood, M., Holme, R., Kamide, Y., Baumjohann, W., ... Liu, S.-L. (2011, 09). The distribution of the ring current: Cluster observations. *Annales Geophysicae*, *29*, 1655-1662. doi: 10.5194/angeo-29-1655-2011